Digest Journal of Nanomaterials and Biostructures

Dig. J. Nanomater. Bios. **2026**; 21(3): 52853
https://doi.org/10.31083/DJNB52853

Original Research

Effects of Vacancy Defects and Dimensionality on the Structure and Electronic Properties of B_4C_3

Yanli Yang[1], Li Shao[2,*], Lamei Zhang[1]

[1]School of Electronics and Information, Zhengzhou University of Light Industry, 450000 Zhengzhou, Henan, China
[2]School of Materials, Zhengzhou University of Aeronautics, 450015 Zhengzhou, Henan, China
*Correspondence: shaoli094@zua.edu.cn (Li Shao)

Academic Editor: Bong-Joong Kim
Submitted: 13 April 2026 Revised: 20 May 2026 Accepted: 29 May 2026 Published: 4 September 2026

Abstract

Background: Monolayer B_4C_3 represents a novel functional material with appealing performance for photocatalysis, lithium-ion battery anodes and hydrogen storage applications. Vacancy defects and structural dimensional modulation are effective strategies to tailor the electronic structures and physicochemical performances of semiconductor materials. However, studies of B_4C_3 in these respects are still inadequate, restricting its further practical utilization. **Methods:** The effects of vacancy defects and dimensionality (two-dimensional monolayer vs. one-dimensional nanoribbon) on the structure and electronic properties of B_4C_3 were investigated using density functional theory. Three defective B_4C_3 models (B monovacancy, C monovacancy, B–C divacancy) were constructed, along with bare and hydrogen-passivated B_4C_3 nanoribbons. Structural stability and electronic properties were systematically analyzed through formation energy, binding energy, band structure, density of states, charge density difference and Hirshfeld population. **Results:** Pristine B_4C_3 is a direct-band-gap semiconductor (1.997 eV). Vacancies induce lattice reconstruction and band gap reduction: C monovacancy decreases the band gap to 1.271 eV, while B and B–C vacancies render B_4C_3 metallic, and B monovacancy possesses the highest thermodynamic stability. All bare B_4C_3 nanoribbons (B_4C_3NRs) exhibit metallicity, whereas hydrogen passivation restores their semiconducting properties. The band gap of passivated B_4C_3NRs declines with increasing width and stabilizes when the width of the nanoribbon is large enough. **Conclusions:** The introduction of vacancy defects reduced the band gap, thereby increasing conductivity, while dimensionality reduction induced a semiconductor-to-metal transition. The hydrogen-passivation of the nanoribbon edge atoms caused a transition to semiconducting behavior irrespective of nanoribbon width. With increasing nanoribbon width, the band gap decreased and stabilized at a certain value.

Keywords: density functional theory (DFT); vacancy defect; dimension change; band structure; density of states (DOS)

1. Introduction

Boron carbide is an important non-metallic ceramic material. Carbon and boron can form various compounds with different stoichiometric ratios and morphologies. Owing to their excellent physical properties [1,2,3], including high thermostability and low density coupled with extraordinary hardness, boron-carbon compounds are widely utilized in military industry such as bulletproof vests and protective equipment [4,5,6,7]. Furthermore, boron carbide demonstrates distinctive chemical and electronic characteristics [8,9,10]. Chen et al. [11] theoretically predicted that the Li decoration on Penta-octagraphene $B_4C_2N_3$ monolayer could achieve high hydrogen storage capacity (8.35 wt %), and effective hydrogen desorption dynamics. Rajkumar et al. [12] experimentally demonstrated that boron-doped graphene can be used as a high-performance electrode material in supercapacitor applications. These outstanding advancements have driven scientists to explore novel functional materials with new structures through experimental and theoretical approaches. For instance, Chang et al. [13] proposed a new B_4C_3 monolayer and it may be used as a promising photocatalyst attributed to its efficient sunlight utilization, rapid migration of photoinduced carriers, and strong redox capacity of activated electrons and holes. Majid et al. [14] theoretically confirm that B_4C_3 is not only a promising anode material for lithium-ion batteries, but also an excellent matrix to store hydrogen [15].

Electronic properties such as band gap, band edge alignment and density of states (DOS) govern the light absorption range, redox capability and carrier separation efficiency. These characteristics are critical determinants of photocatalytic performance, and also serve as key factors affecting its application as battery anode material. Vacancy defects are commonly utilized to modulate the electronic structure of semiconductors [16,17]. These defects modify interatomic bond hybridization patterns and electron localization/delocalization, thereby inducing shifts in band structures and electronic properties. He et al. [18] revealed that the electronic and magnetic properties of β-Ga_2O_3 could be precisely modulated through introducing vacancy defects with controlled charge states. Additionally, variations in material dimensionality and the edge termination (exposed vs. passivated) can induce charge redistribution, thereby influencing their electronic properties [19,20]. Han et al. [21] investigated the impact of edge hydrogenation on the geometry structures, stabilities and elec-

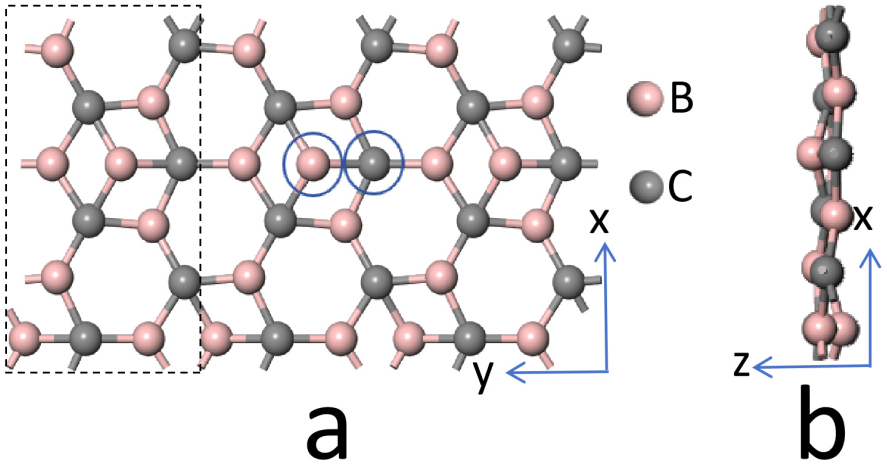

Fig. 1. The structure of a 1 × 3 B_4C_3 supercell. (a) top views, (b) side views. The primitive cell structure of B_4C_3 (delineated by the black rectangular dashed line) and the defect sites (denoted by blue circles).

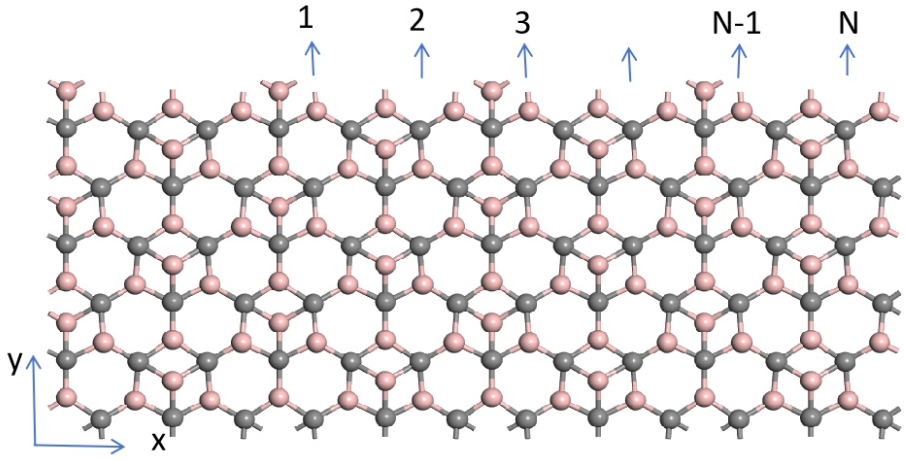

Fig. 2. Structure of B_4C_3NRs. B_4C_3NRs, charge density difference.

tronic properties of zigzag silicene nanoribbons (ZSiNRs) employing a self-consistent charge density functional tight-binding (SCC-DFTB) method. Their findings revealed that after being hydrogen passivated, the degree of warpage of the ZSiNRs is regulated, the system stability is improved and the electrical conductivities of the nanoribbons with different period widths are enhanced.

Utilizing density functional theory (DFT) [22], the effects of vacancy defects and structural dimensionality reduction (from 2D to 1D) on the electronic characteristics of B_4C_3 were investigated. Furthermore, edge passivation effects on B_4C_3 nanoribbons (B_4C_3NRs) were systematically evaluated, with nanoribbon width-dependent size effects being analyzed to establish structure-property relationships in these low-dimensional systems.

2. Calculation Method and Model

The computational simulations were performed using the Vienna Ab Initio Simulation Package (VASP)

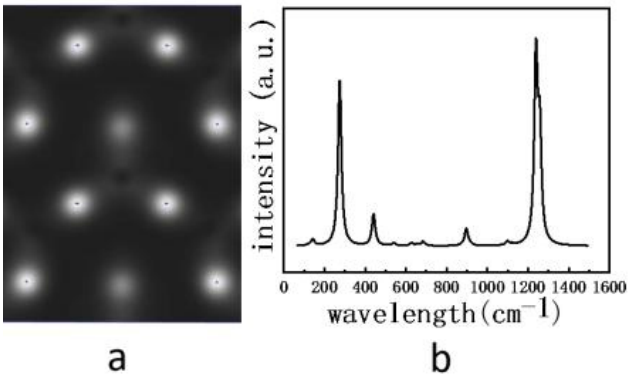

Fig. 3. STM image (a) and Raman spectrum (b) of B_4C_3.

[23,24,25]. The exchange-correlation potential was treated with the Perdew-Burke-Ernzerhof (PBE) functional under the generalized gradient approximation (GGA) [26]. A plane-wave basis set with a cutoff energy of 650 eV was

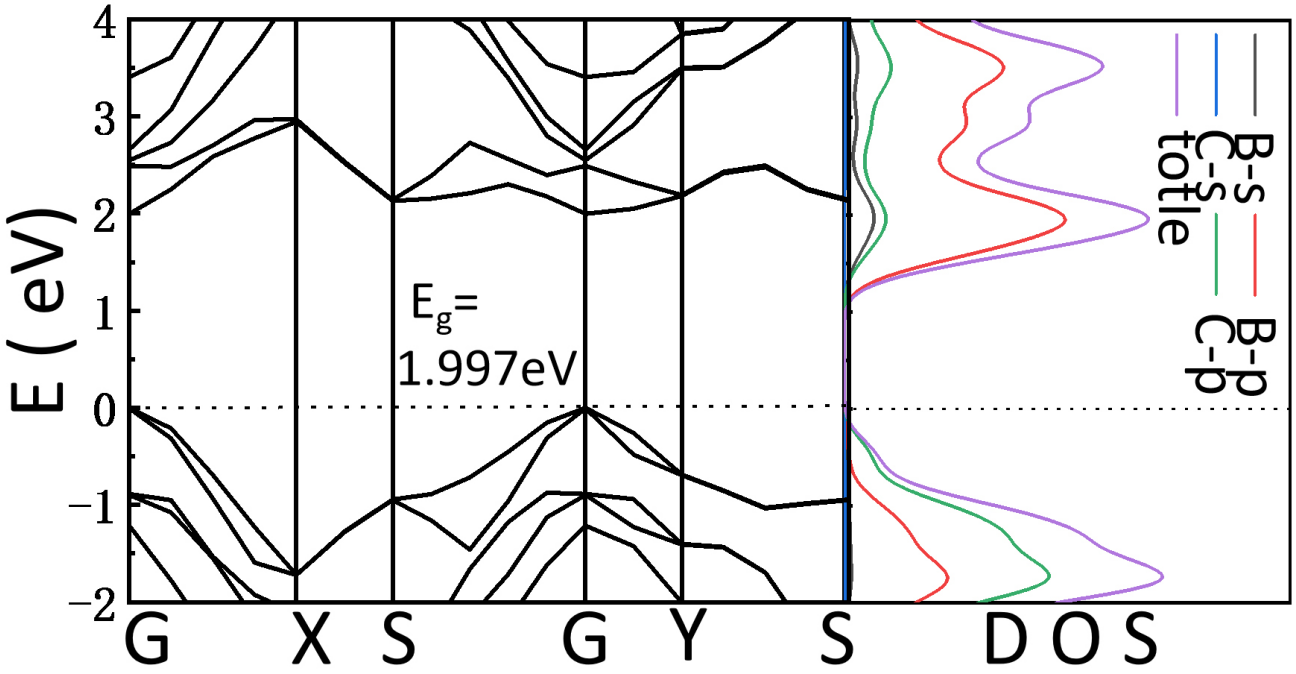

Fig. 4. Energy band structure and DOS of B_4C_3.

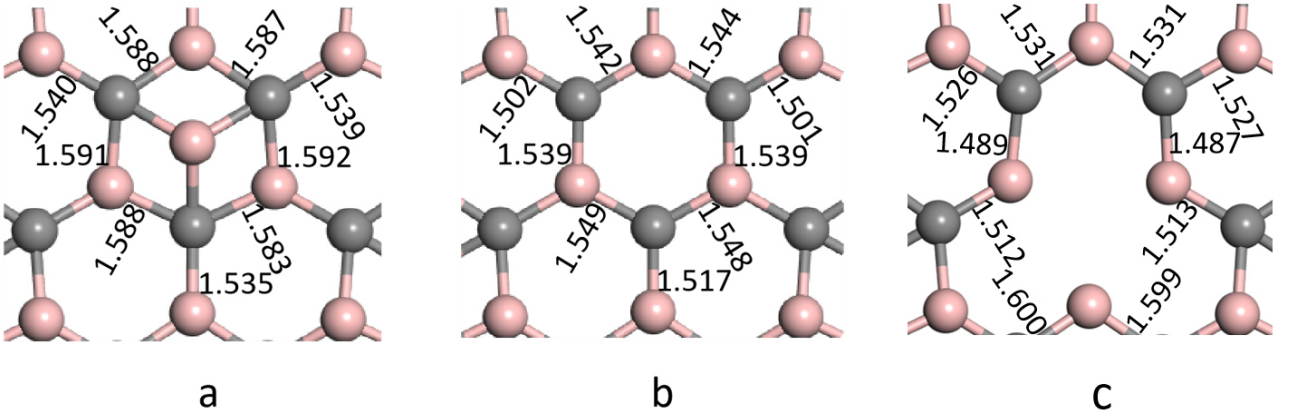

Fig. 5. Comparison of bond-length changes. (a) Pristine structure. (b) Defective structure with B monovacancy. (c) Defective structure with B–C divacancy.

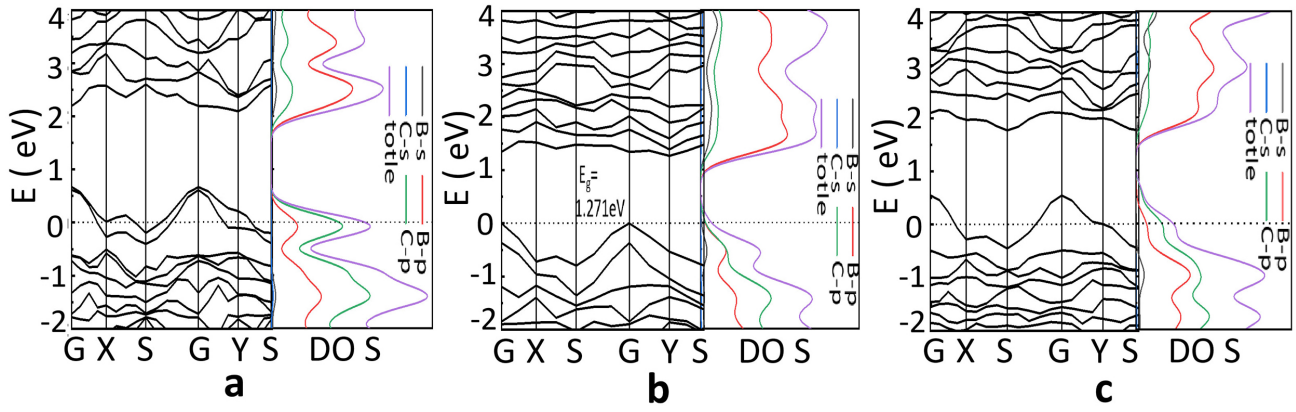

Fig. 6. Band structures and DOS of B_4C_3 with (a) B monovacancy, (b) C monovacancy, (c) B–C divacancy.

Fig. 7. Structure of 5-hB$_4$C$_3$NR.

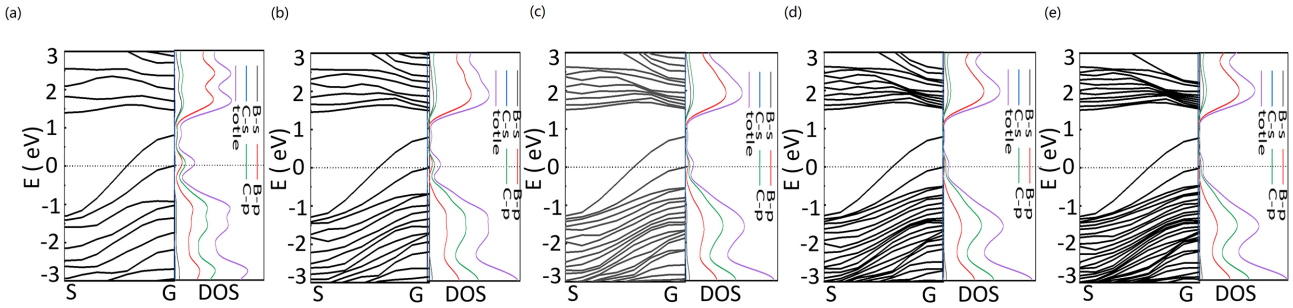

Fig. 8. Band structures and DOSs of N-hB$_4$C$_3$NRs. (a–e) correspond to N = 1, 3, 5, 7, 9, respectively.

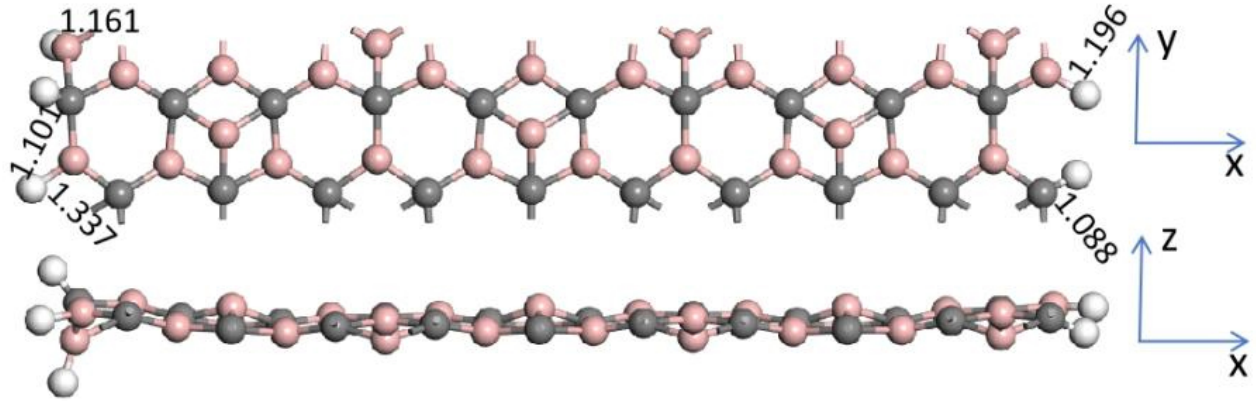

Fig. 9. Top and side views of the structure of 5-hB$_4$C$_3$NR.

employed to ensure numerical convergence. A k-point grid of 2 × 3 × 1 was implemented for reciprocal-space sampling. The defect formation energy E_f, is defined as $E_f = E_{\text{total}} - E_0 + \mu$, where E_{total} and E_0 represent the total energies of B_4C_3 with and without defect, and μ denotes the chemical potential of the removed atoms (B, C or both B and C). The hydrogen passivation binding energy E_c is defined as $E_c = \frac{E_{\text{total}} - E_0 - \frac{m}{2}E_H}{m}$, where E_{total} and E_0 represent the total energies of B_4C_3NRs with hydrogen-passivated and bare edges, E_H is the total energy of a hydrogen molecule, and m is the number of passivating hydrogen atoms. To mitigate artificial interactions arising from periodic boundary conditions, a vacuum layer spanning 20 Å along the z-axis was incorporated.

The primitive cell structure of B_4C_3 is shown in Fig. 1a and marked with the black rectangular dashed line. By cutting out B, C or both atoms at the indicated sites within a 1 × 3 B_4C_3 supercell, whose top and side views of the structure are shown in Fig. 1, we constructed three distinct defect-containing B_4C_3 models: B monovacancy, C monovacancy, and B–C divacancy. Vacancy defect positions are indicated by blue circles.

The B_4C_3 material was sectioned in the x-direction to produce nanoribbons with their width denoted by N, and named as N-B_4C_3NR (Fig. 2). All edge atoms of the B_4C_3NR were passivated with single hydrogen atoms, and following the same nomenclature convention, the hydrogen-passivated counterparts were designated as N-hB$_4$C$_3$NR.

Table 1. The average binding energy of H passivated N-B_4C_3NRs.

Nanoribbon width N	1	2	3	4	5	6	7	8	9
E_c/eV	–1.209	–1.211	–1.208	–1.211	–1.206	–1.211	–1.207	–1.211	–1.207

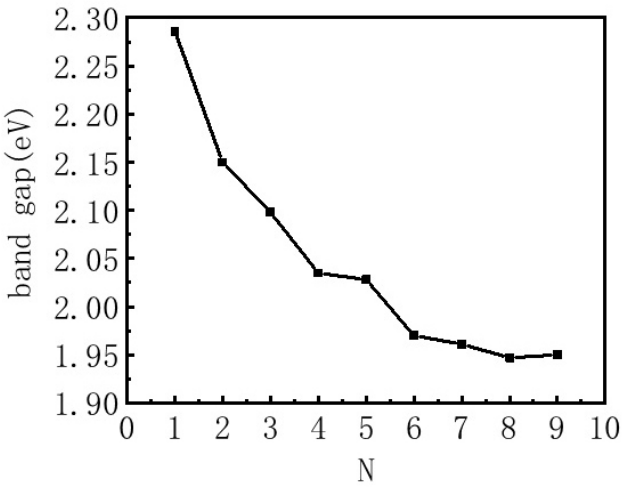

Fig. 10. Band gap variation of N-hB_4C_3NRs with N.

3. Results and Discussion

3.1 Electronic Properties of Pristine B_4C_3

The structure of pristine B_4C_3 monolayer is illustrated in Fig. 1a. Its optimized structural parameters are a = 8.101 Å and b = 4.674 Å, containing eight B and six C atoms in a unit cell. B atoms exhibit tri-coordinated bonding configurations with adjacent C atoms, and in contrast, C atoms form tetra-coordinated bonds with B. The mean B–C bond length is 1.569 Å. Bond angles centered on B atoms show a mean angle of 117.950°, whereas those centered on C atoms is 104.328° on average. Fig. 3a illustrates the hexagonal lattice configuration of the B_4C_3 monolayer derived from scanning tunneling microscopy (STM) modeling [27,28,29]. Raman spectrum for the monolayer, displayed in Fig. 3b, exhibits prominent peaks at approximately 275 and 1240 cm^{-1}, accompanied by minor peaks near 440 and 900 cm^{-1}. These simulated spectra will facilitate future comparisons with experimental results. Fig. 4 details the electronic band structure and projected density of states (PDOS). The monolayer exhibits a direct-band-gap semiconductor behavior with an energy gap of 1.997 eV (PBE functional), which is less than the value of 2.39 eV by the HSE06 method [14]. Both the valence band maximum (VBM) and conduction band minimum (CBM) locate at the Γ point of the Brillouin zone. Analysis indicates that the CBM is mainly contributed by the 2p orbital of B atoms, and the VBM comes from the 2p orbitals of both C and B atoms.

3.2 Structural Stability and Electronic Properties of Defective Configurations

Vacancy defects can influence the geometric configurations of materials. After the creation of B monovacancy, the bond lengths between carbon atoms and their adjacent atoms decreased uniformly (Fig. 5b), with the average value reducing from 1.571 Å to 1.531 Å. For the system with C monovacancy, similarly, the bond lengths between B and the surrounding atoms were calculated. The results indicated that most of them were elongated while a few were shortened, elevating the value from 1.572 Å to 1.596 Å compared to the pristine structure (Fig. 5a). For B–C divacancy, a comparable pattern was observed: the majority of bonds shortened, while a limited proportion elongated, lowering the average value from 1.569 Å to 1.532 Å (Fig. 5c). These findings suggest that the formation of defects induces lone electron pairs in atoms, driving chemical bond reconstruction and subsequent bond length alterations.

To evaluate the stability of vacancy-containing B_4C_3 monolayers, we calculated the defect formation energies [30,31] of B monovacancy, C monovacancy, and B–C divacancy defects within a 1 × 3-unit cell. The formation energy (E_f) is defined by the Eqn. 1 :

$$E_f = E_{\text{total}} - E_0 + \mu \tag{1}$$

where E_{total} and E_0 represent the total energies of B_4C_3 with and without defect, and μ denotes the chemical potential of the removed atoms (B, C or both B and C). Computational results reveal positive formation energies of 8.40 eV, 18.03 eV, and 20.87 eV for B monovacancy, C monovacancy, and B–C divacancy, respectively. These values confirm that defect generation is non-spontaneous and endergonic. Notably, B monovacancy exhibits the minimal formation energy, implying it is the most thermodynamically stable and easiest to form among the three defect types.

Fig. 6 presents the electronic band structures of vacancy-containing B_4C_3 monolayers. The calculated band gap for the C monovacancy configuration is 1.271 eV (Fig. 6b), indicating a significant reduction compared to the pristine B_4C_3 band gap of 1.997 eV (Fig. 4). Both B monovacancy and B–C divacancy configurations exhibit metallic behavior, as evidenced by partially occupied bands crossing the Fermi level within the Brillouin zone. DOS analysis further supports these findings: the vacancy system display narrower band gaps (Fig. 6) than pristine B_4C_3 (Fig. 4), consistent with their band structures. Although the limited supercell size may amplify the influence of defects, the re-

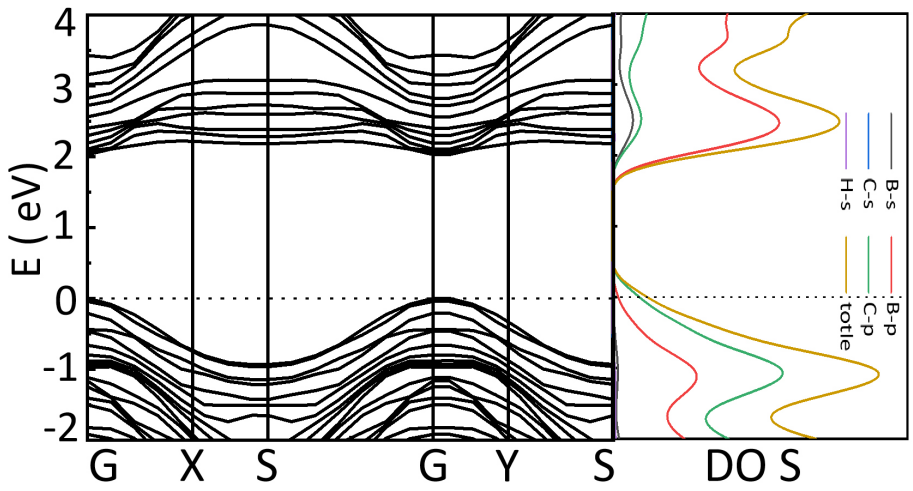

Fig. 11. Band structure and DOS of 5-hB$_4$C$_3$NR.

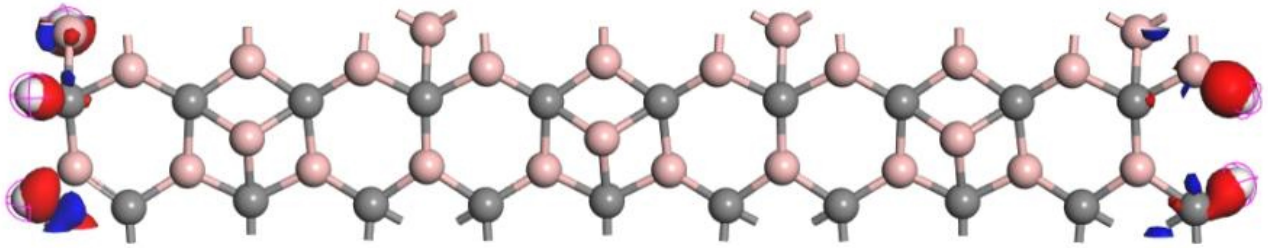

Fig. 12. CDD image of 5-hB$_4$C$_3$NRs. CDD, charge density difference.

sults conclusively demonstrated that vacancy defects can reduce band gap width and enhance electrical conductivity.

3.3 Electronic Properties of B$_4$C$_3$NRs

The electronic properties of B$_4$C$_3$NRs were also investigated by DFT. After geometry optimization, the exposed atoms at the edges rebonded with neighboring atoms. This process generated lone-pair electrons, inducing structural reorganization. As a result, the bond lengths at the edges were reduced compared to the pristine system. For 5-hB$_4$C$_3$NR (width parameter N = 5), a comparative analysis of bond lengths at corresponding positions is provided in Fig. 7.

The band structures and the DOSs of the N-B$_4$C$_3$NRs (N = 1–9) were all calculated, with partial results presented in Fig. 8. All of them exhibit metallic properties and their metallic properties originate from the hybridization of the 2p orbitals of both C and B atoms.

3.4 Electronic Properties of Hydrogen-Passivated B$_4$C$_3$NRs

The effects of the boundary passivation on the electronic properties of B$_4$C$_3$NRs were also studied. Each edge atom in B$_4$C$_3$NRs was passivated with one hydrogen atom. The structure of the hydrogenated 5-hB$_4$C$_3$NR is illustrated in Fig. 9. The calculated average bond lengths for B-H and C-H are 1.231 Å and 1.094 Å, respectively. To evaluate the effects of hydrogen passivation on structural stability, the binding energy, E$_c$ [32], was calculated, which is defined as the Eqn. 2:

$$E_c = \frac{E_{\text{total}} - E_0 - \frac{m}{2}E_H}{m} \quad (2)$$

Where E$_{\text{total}}$ and E$_0$ represent the total energies of B$_4$C$_3$NRs with hydrogen-passivated and bare edges, E$_H$ is the total energy of a hydrogen molecule, and m is the number of passivating hydrogen atoms. As summarized in Table 1, all hydrogenated B$_4$C$_3$NRs (hB$_4$C$_3$NRs) exhibit negative binding energies regardless of width, signifying structural stability after passivation.

After hydrogen passivation, all hB$_4$C$_3$NRs recover semiconducting behavior. The band gaps of hB$_4$C$_3$NRs with varying nanoribbon widths are shown in Fig. 10. The data reveals a progressive narrowing of band gaps with N increase. Notably, for systems with N >7, the band gap stabilizes to a constant value. This trend arises from the transition of hB$_4$C$_3$NRs toward a quasi-two-dimensional structure when N is large enough, accompanied by decreased nanoscale confinement effects.

The band structure and DOS of 5-hB_4C_3NRs are shown in Fig. 11. As illustrated in the figure, the VBM and CBM both locate at the Γ point of the Brillouin zone with an energy gap of 2.028 eV. Near the Fermi level, the H_s orbitals hybridize with the adjacent atoms, forming covalent bonds. This hybridization modifies the electronic properties of the system, inducing a transition from metal to semiconductor of the nanoribbon.

To analyze the charge redistribution of the hydrogen passivated systems, the charge density difference (CDD) was calculated. The CDD is defined as the electronic density difference between hydrogenated B_4C_3NRs and the isolated H atoms as well as B_4C_3NRs at their respective positions. The CDD distribution for 5-hB_4C_3NR, depicted in Fig. 12, illustrates that charge density redistribution occurred predominantly within the C-H and B-H bonding regions. In addition, Hirshfeld population analysis for 5-hB_4C_3NR reveals that among the five passivating hydrogen atoms, the two bonded to B atoms gained 0.04e and 0.05e, while the three bonded to C atoms lost 0.06e, 0.05e, and 0.02e. This behavior originates from the intermediate electronegativity of the H atom. The electronegativities of H, B, and C are 2.20, 2.04, and 2.55, respectively, indicating that H is higher than B but lower than C.

4. Conclusions

By first-principles calculations, we studied and analyzed the influence of vacancy defects and nanoribbons on the 2D B_4C_3. The existence of defects narrowed the band gap of the system and enhanced its conductivity. The reduction of dimensionality (from 2D to 1D) transforms the system from a semiconductor to a metal. After the bare edges of B_4C_3NRs being passivated with H atoms, N-hB_4C_3NRs (N = 1–9) recover semiconductor characteristics. Moreover, as the width of the ribbon increases, the band gap of the B_4C_3NR gradually decreases, and when the ribbon width N exceeds 7, the band gap tends to a constant value.

Availability of Data and Materials

All data generated and analyzed during this study are included in this manuscript. The raw calculation data are available from the corresponding author on request.

Author Contributions

LS and YY designed the research. YY performed the calculations and data analysis. YY wrote the original manuscript, LZ visualized and analyzed the data. All authors revised the manuscript, read and approved the final version, and agreed to be accountable for all aspects of the work.

Acknowledgment

We sincerely thank anonymous reviewers for their valuable comments and constructive suggestions, which greatly improved the quality of this manuscript. We would like to express our gratitude to all those who helped us during the writing of this manuscript.

Funding

This research was financially supported by the Key Research Project of Colleges and Universities in Henan Province (No. 25B140008).

Conflicts of Interest

The authors declare no conflicts of interest.

References

[1] Thévenot F. Boron carbide-a comprehensive review. Journal of the European Ceramic Society. 1990; 6: 205–225. https://doi.org/10.1016/0955-2219(90)90048-K

[2] Raja T, Devarajan Y, Prakash JU, Upadhye VJ, Singh L, Kannan S. Sustainable innovations: Mechanical and thermal stability in palm fiber-reinforced boron carbide epoxy composites. Results in Engineering. 2024; 24: 103214. https://doi.org/10.1016/j.rineng.2024.103214

[3] Du J, Christian K, Yang Q, Hwang C, McAleer E, Haber RA. Thermal stability of dopants in boron carbide. Scripta Materialia. 2022; 206: 114263. https://doi.org/10.1016/j.scriptamat.2021.114263

[4] Molodets AM, Golyshev AA, Shilov GV. Melting of Shocked Boron Carbide. JETP Letters. 2020; 111: 720–726. https://doi.org/10.1134/S0021364020120103

[5] Medvedovski E. Ballistic performance of armour ceramics: Influence of design and structure. Part 1. Ceramics International. 2010; 36: 2103–2115. https://doi.org/10.1016/j.ceramint.2010.05.021

[6] Medvedovski E. Ballistic performance of armour ceramics: Influence of design and structure. Part 2. Ceramics International, 2010; 36: 2117–2127. https://doi.org/10.1016/j.ceramint.2010.05.022

[7] Xu D, Huang Z, Chen G, Ren X, Li D, Zhang Y, et al. Experimental investigation on the ballistic performance of B4C/Aramid/UHMWPE composite armors against API projectile under different temperatures. Thin-Walled Structures. 2024; 196: 111553. https://doi.org/10.1016/j.tws.2023.111553

[8] Ahir NA, Amate RU, Morankar PJ, San Kim K, Jeon CW. Unveiling the potential of high-temperature chemical vapour deposition growth of boron carbide: Investigating physicochemical, mechanical and electrical properties. Ceramics International. 2024; 50: 39088–39096. https://doi.org/10.1016/j.ceramint.2024.07.275

[9] Schwetz KA, Karduck P. Investigations in the boron-carbon system with the aid of electron probe microanalysis. Journal of the Less Common Metals, 1991; 175: 1–11. https://doi.org/10.1016/0022-5088(91)90345-5

[10] Werheit H, Herstell B, Winkelbauer W, Pristáš G, Gabani S, Flachbart K, et al. Electrical conductivity of boron carbide from ~5 to ~2100 K in the whole homogeneity range. Solid State Sciences. 2022; 132: 106987. https://doi.org/10.1016/j.solidstatesciences.2022.106987

[11] Chen X, Wang J, Martins NF, Sambrano JR, Laranjeira JAS. Penta-Octa $B_4C_2N_3$: A New 2D Material for High-Performance Energy Applications. Langmuir : the ACS journal of surfaces and colloids. 2025; 41: 5477–5487. https://doi.org/10.1021/acs.langmuir.4c05139

[12] Rajkumar P, Diwakar K, Ramachandran M, Mozaffar A, Gnanamuthu RM, Subadevi R, et al. Enriched energy storage capa-

bility and bi-functional ability of boron-doped graphene as efficient electrode for supercapacitors and lithium sulfur batteries. Journal of Materials Science: Materials in Electronics, 2021; 32: 22760–22770. https://doi.org/10.1007/s10854-021-06650-7

[13] Chang H, Tu K, Zhang X, Zhao J, Zhou X, Zhang H. B4C3 Monolayer with Impressive Electronic, Optical, and Mechanical Properties: A Potential Metal-Free Photocatalyst for CO2 Reduction under Visible Light. Journal of Physical chemistry C. 2019; 123: 25091–25101. https://doi.org/10.1021/acs.jpcc.9b06744

[14] Majid A, Najam U, Ahmad S, Alkhedher M. On the prospects of using B4C3 as a potential electrode material for lithium-ion batteries. Materials Science in Semiconductor Processing. 2024; 176: 108320. https://doi.org/10.1016/j.mssp.2024.108320

[15] Qayyum MN, Majid A, Khan MI, Alkhedher M, Haider S, Alam K. Enhanced hydrogen storage in alkali metal-decorated B4C3: A pathway towards high-capacity hydrogen storage. International Journal of Hydrogen Energy. 2025; 155: 150303. https://doi.org/10.1016/j.ijhydene.2025.150303

[16] Geng K, Cheng P, Luo H, Kong C, Qing X, Su Y, et al. First-principles study on intrinsic point defects properties in CaCu3Ti4O12. Computational Materials Science. 2025; 246: 113364. https://doi.org/10.1016/j.commatsci.2024.113364

[17] Xiao H, Zhao S, Liu Q, Li Y, Zhao S, Luo F, et al. Point defect properties in high entropy MAX phases from first-principles calculations. Acta Materialia. 2023; 248: 118783. https://doi.org/10.1016/j.actamat.2023.118783

[18] He X, Wang M, Meng J, Hu J, Jiang Y. The effect of vacancy defects on the electronic properties of β-Ga2O3. Computational Materials Science. 2022; 215: 111777. https://doi.org/10.1016/j.commatsci.2022.111777

[19] Yang L, Chen M, Chen C, Lan Q. Photogalvanic effect in spin-polarized zigzag antimonene nanoribbon with Cr and Co edge-modification. Physica E: Low-Dimensional Systems and Nanostructures. 2023; 145: 115508. https://doi.org/10.1016/j.physe.2022.115508

[20] Shao L, Chen G, Ye H, Niu H, Wu Y, Zhu Y, et al. Sulfur dioxide molecule sensors based on zigzag graphene nanoribbons with and without Cr dopant. Physics Letters A, 2014; 378: 667–671. https://doi.org/10.1016/j.physleta.2013.12.042

[21] Han Y, Wu L, Wang Z, Wang S. Effects of edge hydrogenation and applied electric field on the structure and electrical properties of zigzag silicene nanoribbons by SCC-DFTB calculations. Physica B: Condensed Matter. 2023; 649: 414445. https://doi.org/10.1016/j.physb.2022.414445

[22] Maqsooda S, Mumtazb S, Alanazi YM. Opto-electronic and thermoelectric properties of double perovskites Na2AgGaY6 (Y = Cl, Br, I) for energy conversion applications: DFT calculations. Digest Journal of Nanomaterials and Biostructures. 2024; 19: 919–931. https://doi.org/10.15251/DJNB.2024.192.919

[23] Kresse G, Hafner J. Ab initio molecular dynamics for liquid metals. Physical Review. B. 1993; 47: 558. https://doi.org/10.1103/PhysRevB.47.558

[24] Kresse G, Furthmüller J. Efficient iterative schemes for ab initio total-energy calculations using a plane-wave basis set. Physical Review. B, Condensed Matter. 1996; 54: 11169–11186. https://doi.org/10.1103/physrevb.54.11169

[25] Kresse G, Furthmüller J. Efficiency of ab-initio total energy calculations for metals and semiconductors using a plane-wave basis set. Computational Materials Science, 1996; 6: 15–50. https://doi.org/10.1016/0927-0256(96)00008-0

[26] Perdew J, Burke K, Ernzerhof M. Generalized Gradient Approximation Made Simple. Physical Review Letters. 1996; 77: 3865–3868. https://doi.org/10.1103/PhysRevLett.77.3865

[27] Costina I, Schmid M, Schiechl H, Gajdoš M, Stierle A, Kumaragurubaran S, et al. Combined STM, LEED and DFT study of Ag(100) exposed to oxygen near atmospheric pressures. Surface Science, 2006; 600: 617–624. https://doi.org/10.1016/j.susc.2005.11.020

[28] Ossowski T, Wang Y, Carraro G, Kiejna A, Lewandowski M. Structure of mono- and bilayer FeO on Ru(0001): STM and DFT study. Journal of Magnetism and Magnetic Materials. 2022; 546: 168832. https://doi.org/10.1016/j.jmmm.2021.168832

[29] Tjung SJ, Zhang Q, Repicky JJ, Yuk SF, Nie X, Santagata NM, et al. STM and DFT studies of CO2 adsorption on O-Cu(100) surface. Surface Science. 2019; 679: 50–55. https://doi.org/10.1016/j.susc.2018.08.013

[30] Kerr RD, Gilbert MR, Murphy ST. Relating the formation energies for oxygen vacancy defects to the structural properties of tungsten oxides. Computational Materials Science. 2025; 252: 113781. https://doi.org/10.1016/j.commatsci.2025.113781

[31] Chizmeshya AVG, Masoumi N. Composition and strain dependence of intrinsic and substitutional defect formation energies in SnxGe1−x alloys. Results in Surfaces and Interfaces. 2023; 12: 100125. https://doi.org/10.1016/j.rsurfi.2023.100125

[32] Gao J, Yu W, Liu J, Qin L, Cheng H, Cui X, et al. Regulation of hydrogen binding energy via oxygen vacancy enables an efficient trifunctional Rh-Rh_2O_3 electrocatalyst for fuel cells and water splitting. Journal of Colloid and Interface Science. 2024; 664: 766–778. https://doi.org/10.1016/j.jcis.2024.03.095